Ion cyclotron range of frequency heating experiments on the large helical device and high energy ion behavior

journal or publication title	Physics of Plasmas
volume	Vol.8
number	Issue 5
page range	pp.2139-2147
year	2001-05-01
URL	http://hdl.handle.net/10655/3883

doi: 10.1063/1.1354152

Ion cyclotron range of frequency heating experiments on the large helical device and high energy ion behavior*

R. Kumazawa,[†,a)] T. Mutoh, T. Seki, T. Watari, K. Saito,[b)] Y. Torii,[b)] F. Shimpo, G. Nomura, M. Yokota, A. Kato, D. A. Hartmann,[c)] Y. Zhao,[d)] A. Fukuyama,[e)] H. Okada,[f)] K. Ohkubo, M. Sato, S. Kubo, T. Shimozuma, H. Idei, Y. Yoshimura, T. Notake,[b)] Y. Takita, S. Kobayashi, S. Itoh, Y. Mizuno, O. Kaneko, Y. Takeiri, Y. Oka, K. Tsumori, M. Osakabe, K. Ikeda, S. Yamamoto,[b)] T. Kawamoto, E. Asano, N. Ohyabu, K. Kawahata, A. Komori, H. Yamada, K. Akaishi, N. Ashikawa,[g)] M. Emoto, H. Funaba, M. Goto, K. Ida, S. Inagaki, N. Inoue, M. Isobe, A. Krasilnikov,[h)] S. Masuzaki, T. Minami, J. Miyazawa, T. Morisaki, S. Morita, S. Murakami, S. Muto, Y. Nakamura, Y. Nagayama, H. Nakanishi, K. Narihara, Y. Narushima, K. Nishimura, N. Noda, T. Kobuchi,[g)] S. Ohdachi, T. Ozaki, B. J. Peterson, A. Sagara, S. Sakakibara, R. Sakamoto, H. Sasao,[g)] M. Sasao, K. Sato, M. Shoji, H. Suzuki, K. Tanaka, K. Toi, T. Tokuzawa, I. Yamada, S. Yamaguchi, M. Yokoyama, K-Y. Watanabe, T. Watanabe, K. Matsuoka, K. Itoh, S. Sudo, K. Yamazaki, Y. Hamada, O. Motojima, M. Fujiwara, and the LHD Experimental Group
National Institute for Fusion Science, Toki 509-5292, Japan

(Received 23 October 2000; accepted 17 January 2001)

Ion cyclotron range of frequency (ICRF) heating experiments on the Large Helical Device (LHD) [O. Motojima *et al.* Fus. Eng. Des. **20**, 3 (1993)] achieved significant advances during the third experimental campaign carried out in 1999. They showed significant results in two heating modes; these are modes of the ICH-sustained plasma with large plasma stored energy and the neutral beam injection (NBI) plasma under additional heating. A long-pulse operation of more than 1 minute was achieved at a level of 1 MW. The characteristics of the ICRF heated plasma are the same as those of the NBI heated plasma. The energy confinement time is longer than that of International Stellarator Scaling 95. Three keys to successful ICRF heating are as follows: (1) an increase in the magnetic field strength, (2) the employment of an inward shift of the magnetic axis, (3) the installation of actively cooled graphite plates along the divertor legs. Highly energetic protons accelerated by the ICRF electric field were experimentally observed in the energy range from 30 to 250 keV and the tail temperature depended on the energy balance between the wave heating and the electron drag. The transfer efficiency from the high energy ions to the bulk plasma was deduced from the increase in the energy confinement time due to the high energy ions in the lower density discharge, which agrees fairly well with the result obtained by the Monte Carlo simulation. The transfer efficiency is expected to be 95% at an electron density of more than $n_e = 5.0 \times 10^{19}\,\mathrm{m}^{-3}$ even in the high power heating of 10 MW. The accumulation of impurities, e.g., FeXVI and OV was not observed in high rf power and long pulse operation. The well-defined divertor intrinsic to LHD is believed to be useful in reducing the impurity influx. © *2001 American Institute of Physics*. [DOI: 10.1063/1.1354152]

I. INTRODUCTION

One of the major concerns of the Large Helical Device (LHD) project is whether the ion cyclotron range of frequency (ICRF) heating in helical systems works well, can sustain the plasma in a steady state and whether high energy ions can be confined well or not. In the third experimental campaign of 1999 the ICRF heating experiment provided an answer to this concern.[1]

The LHD is the largest super-conducting heliotron-type device with $1/m = 2/10$ continuous helical coils. The main physical research is the investigation of currentless and disruption-free steady-state plasmas. The objective of the LHD project is to research several critical issues in order to realize the helical plasma discharge of steady-state operation at the high performance.[2–4] The major and minor radii are 3.9 m and 0.6 m, respectively, and the designed toroidal magnetic field strength is 3 T.

In the third campaign, the LHD experiments achieved several remarkable improvements: (1) A maximum plasma

*Paper UI1 5, Bull. Am. Phys. Soc. **45**, 290 (2000).
[†]Invited speaker.
[a)]Electronic mail: kumazawa@nifs.ac.jp
[b)]Also at Nagoya University, Faculty of Engineering, Nagoya, 464-8601, Japan.
[c)]Also at Max-Planck-Institute für Plasmaphysik, D-85748 Garching, Germany.
[d)]Also at the Academia Sinica Plasma Physics Institute, Hefei 230031, People's Republic of China.
[e)]Also at Kyoto University, Kyoto, 606-8501, Japan.
[f)]Also at Kyoto University, Uji, Kyoto, 611-0011, Japan.
[g)]Also at The Graduate University for Advanced Studies, Toki, 509-5292, Japan.
[h)]Also at the Troitsk Institute for Innovating and Fusion Research, Troitsk, Russia.

stored energy of 0.88 MJ was attained with the heating power (4.7 MW) of neutral beam injection (NBI) and ICRF heating. (2) The maximum energy confinement time was 0.3 seconds. (3) The highest electron and ion temperatures were 4.4 keV and 3.3 keV. (4) Long-pulse operations lasting more than 1 minute were obtained using NBI only and using ICRF heating only. (5) The maximum beta value was 2.4%. (6) The maximum electron density was $1.1\times10^{20}\,\mathrm{m}^{-3}$ with the hydrogen pellet injection.[5,6]

The final goal of the ICRF heating on the LHD is high power heating of 10 MW and plasma sustainment in steady state at 3 MW. Technology development for high power and steady-state ICRF heating has been carried out for several years.[7–12]

In the second experimental campaign, ICRF heating experiments were carried out in helium plasma with minority hydrogen ions using a pair of loop antennas at the magnetic field strength $B=1.5\,\mathrm{T}$ of the standard configuration, i.e., $R_{\mathrm{ax}}=3.75\,\mathrm{m}$. The increase in the plasma stored energy was proportional to the applied ICRF heating power up to 300 kW. The maximum increase was found to be 13 kJ at $P_{\mathrm{ICH}}=300\,\mathrm{kW}$, which was the same amount as that with electron cyclotron heating (ECH) only.[13,14] However, the plasma could not be sustained by ICRF heating only.

The third experimental campaign was carried out in 1999.[1,15] The magnetic field strength was increased to $B=2.75\,\mathrm{T}$ and the inward-shift of the magnetic axis to $R_{\mathrm{ax}}=3.6\,\mathrm{m}$ was mostly employed. The carbon plates were installed at the helical divertor legs, and this was useful for reducing the impurity penetration in the case of ICRF heated plasma. In this paper, the ICRF heating experimental results and the behavior of high energy protons accelerated by the ICRF wave field are described. In Sec. II, the ICRF heating mode and the ICRF heating experimental setup, including a pair of loop antennas and an impedance matching system, are described. In Sec. III, several ICRF heating experimental results are reported. In Sec. IV, the behavior of high energy protons is introduced and the ICRF heating efficiency is discussed. Then we summarize the ICRF heating experiments on the LHD and mention the future plan in Sec. V.

II. EXPERIMENTAL SETUP AND ICRF HEATING MODE

A. Experimental setup

The antenna is 60 cm in length, 46 cm in width and 17 cm in depth. The antenna strap is 30 cm in width. The surface of the antenna is fitted to a configuration of the last closed magnetic surface. The position of the ion cyclotron heating (ICH) antenna can be shifted inward by 15 cm by using a swing mechanism. All the components of the antenna, i.e., the Faraday shield, side limiters, antenna strap, back plate, and inner and outer conductors are cooled by purified water.[1] The rf power is transmitted to each antenna from the high power radio frequency (rf) generator via a liquid impedance matching system. It consists of three liquid stub tuners, which are identical.[9] All the rf components of the transmission lines, including the liquid stub tuners and the ceramic feed-through, are cooled by purified water to achieve a high rf power steady-state operation.

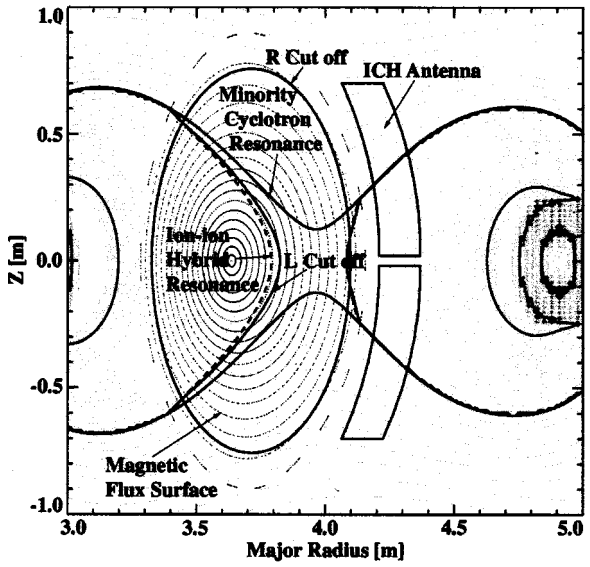

FIG. 1. ICRF heating mode referred to as Mode I: Locations of ion cyclotron resonance of minority ions, ion–ion hybrid resonance, R cutoff, and L cutoff are plotted in the case of the electron density of $n_e(0)=1.0\times10^{19}\,\mathrm{m}^{-3}$, $n_H/n_e=10\%$, $B=2.75\,\mathrm{T}$, and $f=38.47\,\mathrm{MHz}$.

An optical measurement method is employed to estimate the ratio of the hydrogen minority ions. Spectroscopic apparatuses are installed at the vacuum port adjacent to the ICH antenna to monitor Hα (656.3 nm) and HeI (587.6 nm) signals.

Hydrogen or helium glow discharge cleaning was carried out everyday for the wall conditioning after the plasma experiment was over. A titanium gettering, which covered about 30% of the LHD vacuum vessel surface, was employed in the middle of this experimental campaign; consequently the oxygen impurity was remarkably reduced. It was routinely carried out for an hour just before the experiment started. The vacuum base pressure was maintained in the order of $10^{-6}\,\mathrm{Pa}$.

B. ICRF heating mode

The ICRF heating efficiency depends mainly on the location of the minority ion cyclotron resonance and the ion–ion hybrid resonance layers. Figure 1 shows the typical heating scenario referred to as Mode-I, in which the ICRF heating experiments were mainly carried out in the third campaign. The minority cyclotron resonance, L (left hand) cutoff, R (right hand) cutoff, and ion–ion hybrid resonance (in dotted line) layers are plotted in Fig. 1. Here the magnetic field strength, the frequency and the wave number are $B=2.75\,\mathrm{T}$, $f=\omega/2\pi=38.47\,\mathrm{MHz}$ and $k_{\parallel}=5\,\mathrm{m}^{-1}$, respectively. The plasma parameters are a central electron density, $n_e(0)=1.0\times10^{19}\,\mathrm{m}^{-3}$ and a minority hydrogen ratio of 10% in the helium plasma. The ion–ion hybrid resonance is located between the magnetic axis and the minority ion cyclotron resonance, which is the same configuration as in the Compact Helical Stellerator (CHS) experiment.[16,17] As the ratio of hydrogen ions to helium ions becomes higher, the hybrid resonance layer moves toward the magnetic axis. When the frequency is decreased or the magnetic field

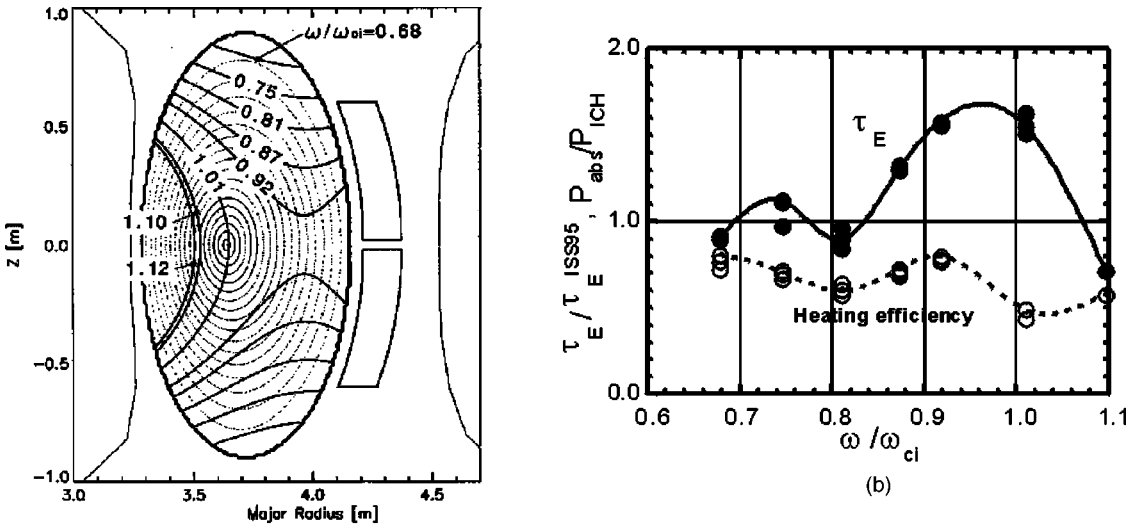

FIG. 2. (a) Various minority ion cyclotron resonance layer in ICRF heating experiments is denoted by the ratio of an applied frequency to an cyclotron frequency on the magnetic axis ω/ω_{ci}. (b) Dependence of $\tau_E/\tau_E^{\mathrm{ISS95}}$ and heating efficiency on ω/ω_{ci}.

strength is increased, the ion cyclotron resonance layer moves toward the lower magnetic field [see $\omega/\omega_{\mathrm{ci}}=0.68$, 0.75 and 0.81 in Fig. 2(a)]. In accordance with the shift of the cyclotron resonance layer, the ion–ion hybrid resonance layer also moves to the lower magnetic field side and is separated into two layers; that is referred to as Mode-II.

III. EXPERIMENTAL RESULTS

A. Optimization of ICRF heating

The characteristics of ICRF heating in helical devices are thought to be different from those in tokamaks because of the difference of the magnetic field configuration. A series of experiments was carried out in order to optimize the ICRF heating by scanning the magnetic field strength, the applied frequency and the minority ion concentration. The situation in which the fast wave accesses to the resonance layers is drastically changed, when the minority ion cyclotron resonance layer is shifted, as shown in Fig. 2(a). In the cases of $\omega/\omega_{\mathrm{ci}}=0.68$, $=0.75$, and $=0.81$, the fast wave directly approaches the ion–ion hybrid resonance layer and the wave energy is efficiently transferred to electrons via the mode converted Ion Bernstein Wave (IBW). The fraction of power absorbed by electrons to the total absorbed rf power, $P_{\mathrm{ele}}/P_{\mathrm{abs}}$, was employed as the most appropriate figure to facilitate the physical understanding. $P_{\mathrm{ele}}/P_{\mathrm{abs}}$ was observed at 100% at $\omega/\omega_{\mathrm{ci}}=0.68$ and gradually decreased in the cases of $\omega/\omega_{\mathrm{ci}}=0.75$ and $=0.81$.[18] On the contrary, the ion heating becomes dominant in the cases of $\omega/\omega_{\mathrm{ci}}=0.92$ and $\omega/\omega_{\mathrm{ci}}=1.01$. This phenomenon was explained by considering how much a fraction of the fast wave directly accesses to the ion–ion hybrid resonance layer.[18]

In Fig. 2(b), the energy confinement time normalized by International Stellarator Scaling 95 (ISS95),[19] $\tau_E/\tau_E^{\mathrm{ISS95}}$ is plotted with solid circles in seven cases. In the cases of $\omega/\omega_{\mathrm{ci}}=0.68$, $=0.75$ and $=0.81$, $\tau_E/\tau_E^{\mathrm{ISS95}}$ is about 1 and the maximum values of more than 1.5 were obtained in $\omega/\omega_{\mathrm{ci}}=0.92$ and $=1.01$. It is noted that the optimal confinement was attained when the heating power deposition was located near the magnetic axis. In this figure, the ICRF heating efficiency is also plotted using open circles. A higher heating efficiency is observed at $\omega/\omega_{\mathrm{ci}}=0.68$ (electron heating) and $\omega/\omega_{\mathrm{ci}}=0.92$ (ion heating). The fact that a higher heating efficiency is obtained in $\omega/\omega_{\mathrm{ci}}=0.92$ than in $\omega/\omega_{\mathrm{ci}}=1.01$ can be explained by two reasons: One is effective power absorption via cyclotron resonance heating. The ion heating can be optimized when the minority ion cyclotron resonance layer is located at the saddle point, i.e., the gentle gradient of the magnetic field strength, which is characterized by the helical magnetic configuration.[18] The other is the better confinement of the high energy ions in $\omega/\omega_{\mathrm{ci}}=0.92$, which will be described in Sec. IV A. The best plasma performance can be obtained in $\omega/\omega_{\mathrm{ci}}=0.92$ because of the higher energy confinement time and the heating efficiency.

B. ICH sustained plasma

The plasma was sustained by injecting ICRF heating power only. An initial plasma was started by fundamental electron cyclotron heating (ECH, 82.6 and 84.0 GHz with 0.4–0.5 MW). The ICRF heating power was applied to the ECH plasma 0.1–0.2 seconds before the turning-off of the ECH. After the ECH was turned off the plasma could be sustained by an ICRF heating larger than 0.2 MW. The ratio of the hydrogen to helium ions, Hα/HeI is also a key to optimizing the ICRF heating.

A typical discharge of the ICH-sustained plasma with $P_{\mathrm{ICH}}=1.3$ MW is shown in Fig. 3. The average line electron density is $n_e=1.8\times10^{19}\,\mathrm{m}^{-3}$ with a stored plasma energy of 200 kJ. In this operation, the intensity ratio of Hα to HeI was maintained between 0.8 and 0.7, which was converted to about 10% of the hydrogen ion minority ratio to the electron density. The electron density was adjusted by using a helium gas puffing. The hydrogen ion density was maintained by the

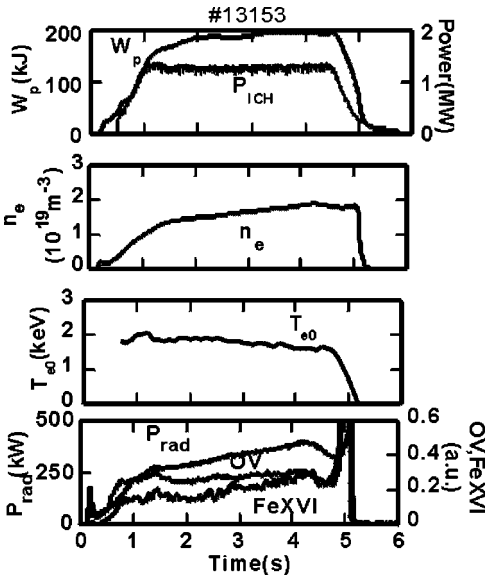

FIG. 3. Time evolutions of parameters of the plasma sustained by ICRF heating only with $P_{\mathrm{ICH}}=1.3$ MW.

recycling from the vacuum wall. The electron temperature was 1.7 keV at the magnetic axis. The radiated power was observed to be $P_{\mathrm{rad}}=250-300$ kW during the ICRF heating. The parameters of the ICH-sustained plasma were similar to those of the neutral beam injection (NBI) plasma with the same absorbed power level, which will be introduced in Sec. III D.

C. Additional ICRF heating to NBI heated plasma

The ICRF heating was applied to the negative-based NBI plasma with the hydrogen pellet injection at the electron density of $n_e=10\sim 8\times 10^{19}\,\mathrm{m}^{-3}$ as shown in Fig. 4. The plasma stored energy reaches 760 kJ at an ICRF heating power of 0.76 MW and an NBI power of 3.5 MW. An increase in the plasma stored energy is observed to be about 50 kJ during the ICRF heating. To clarify the additional ICRF

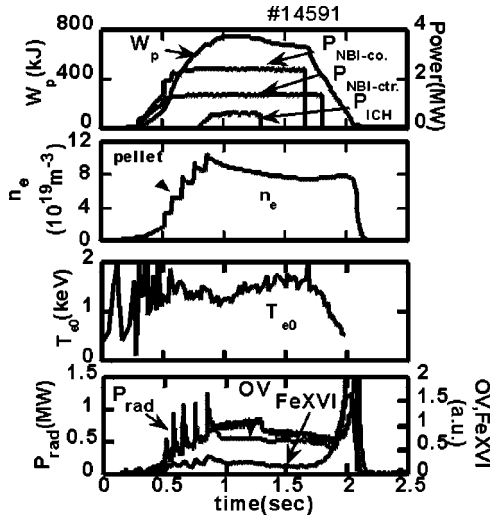

FIG. 4. Time evolutions of plasma parameters of the additional ICRF heating to the NBI heated plasma with the hydrogen pellet injection.

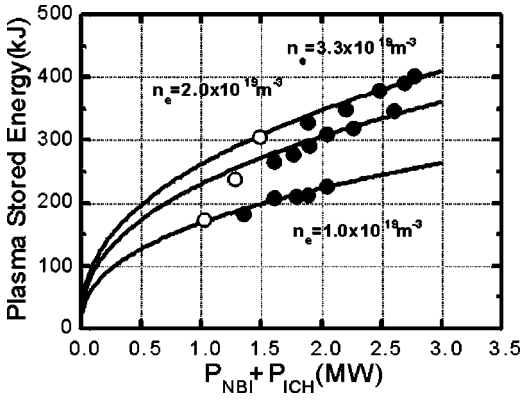

FIG. 5. The dependence of the plasma stored energy on the total heating power, $P_{\mathrm{NBI}}+P_{\mathrm{ICH}}$ for the three different electron densities. Open and solid circles indicate the plasma stored energy with NBI heating only and with the additional ICRF heating, respectively.

heating effect, a series of the experiments was conducted using three different electron densities, i.e., $n_e=1.0\times 10^{19}\,\mathrm{m}^{-3}$, $2.0\times 10^{19}\,\mathrm{m}^{-3}$ and $3.3\times 10^{19}\,\mathrm{m}^{-3}$. The counter-injection of NBI was used and the port-through power of NBI was almost constant at $P_{\mathrm{pt}}=1.45$ MW ($E_{\mathrm{inj}}=130$ keV) in the series of experiments. The absorbed power of NBI is calculated by measurement of the temperature increase of the armor tiles with and without plasma.[20] On the other hand, the rf power absorbed by the plasma can be estimated by the decay of the plasma stored energy. The heating efficiency was 80–85%. The radial distribution of radiated power in the additional ICRF heated plasma was the same that of the NBI heated plasma, which was measured by a multi-channel bolometer array.[21] The radiated power increased with an additional ICRH heating power. The dependence of the plasma stored energy on the total heating power was plotted in Fig. 5, where open and solid circles represent the NBI plasma alone and the NBI-ICRF heated plasma, respectively. These experimental data can be compared with the calculated plasma stored energy by solid lines using a power dependence of ISS95 with enhancement factors, i.e., 1.4–1.6. It is found that the ICRF heating is comparable with the NBI heating.

D. A comparison of ICH-sustained plasma with NBI heated plasma

In the previous section, it was shown that the ICRF heating has the same heating quality as that of the NBI heating in the case of the additional ICRF heating. Here the ICRF heated and sustained plasma is directly compared with the NBI heated plasma, selecting discharges with the same heating power and the same line average electron density. The time evolutions of various plasma parameters of ICRF heated plasma (a) and NBI heated plasma (b) are shown in Fig. 6: The absorbed heating power is 1 MW in both cases. The electron density was $n_e=1.0\times 10^{19}\,\mathrm{m}^{-3}$ as shown in Fig. 6. The measured plasma stored energy of ICRF heated plasma was the same as that of NBI heated plasma, i.e., 170 kJ. Comparing the radiated power of the ICRF heated plasma measured by bolometer array, it was observed to be larger

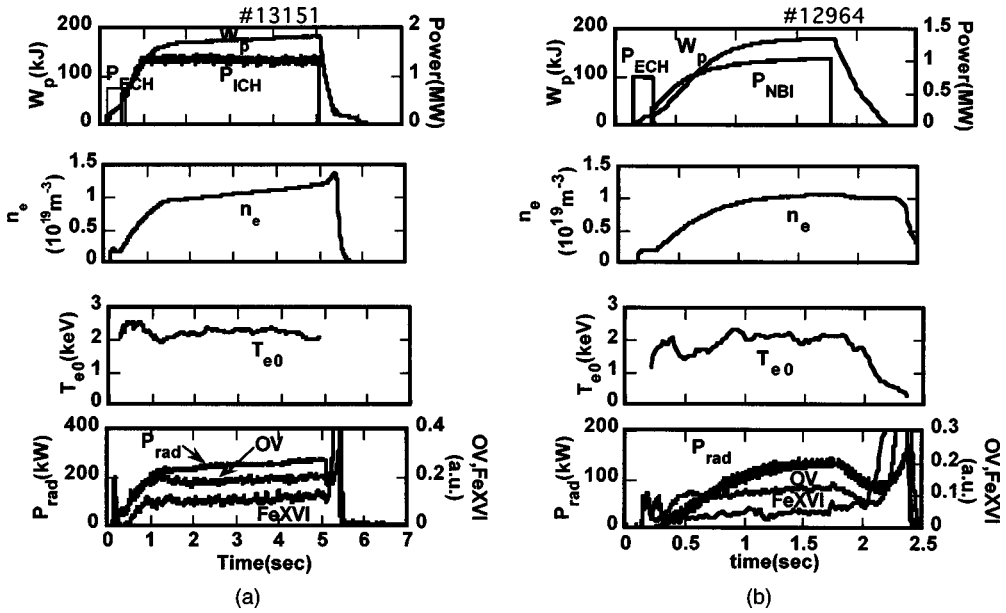

FIG. 6. A comparison of ICRF heated plasma with NBI heated plasma. (a) Time evolutions of parameters of ICRF heated plasma with ICRF heating power. (b) Time evolutions of parameters of NBI heated plasma with NBI power.

than that of the NBI heated plasma. The time evolutions of the impurity radiation, i.e., OV and FeXVI are also plotted in Fig. 6 and the line radiation intensity is larger than that of the NBI plasma by a factor of 2.

The radial profiles of the electron density, radiation power and the electron temperature are compared with those of the NBI heated plasma. The electron temperature was measured by a YAG laser Thomson scattering system with 120 channel detectors, in which the spatial resolution is several mm[22] and the electron density was measured by 13 channels of a far infrared (FIR) laser interferometer.[23] These radial profiles are shown in Fig. 7(a) for the ICRF heated plasma at 4 seconds and in Fig. 7(b) for the NBI heated plasma at 1.5 seconds. It is readily seen that these profiles are quite similar and that the ICRF heating could have the same heating quality as the NBI heating; as the heat deposition profile in the ICRF heating is not obtained, the detail characteristics of the confinement is not discussed. The radial radiated power profile is a similar distribution to that of NBI heated plasma as shown in Figs. 7(a) and 7(b); however the radiation power is larger than in the NBI plasma.

The energy confinement time is compared between three different plasmas, i.e., ICH-sustained, NBI-sustained and the ICRF additional heating referred as to ICH+NBI. These confinement times are compared with ISS95 and the improvement factor is found to be over 1.5 in the three different plasmas. It is found to be a little larger at the lower energy

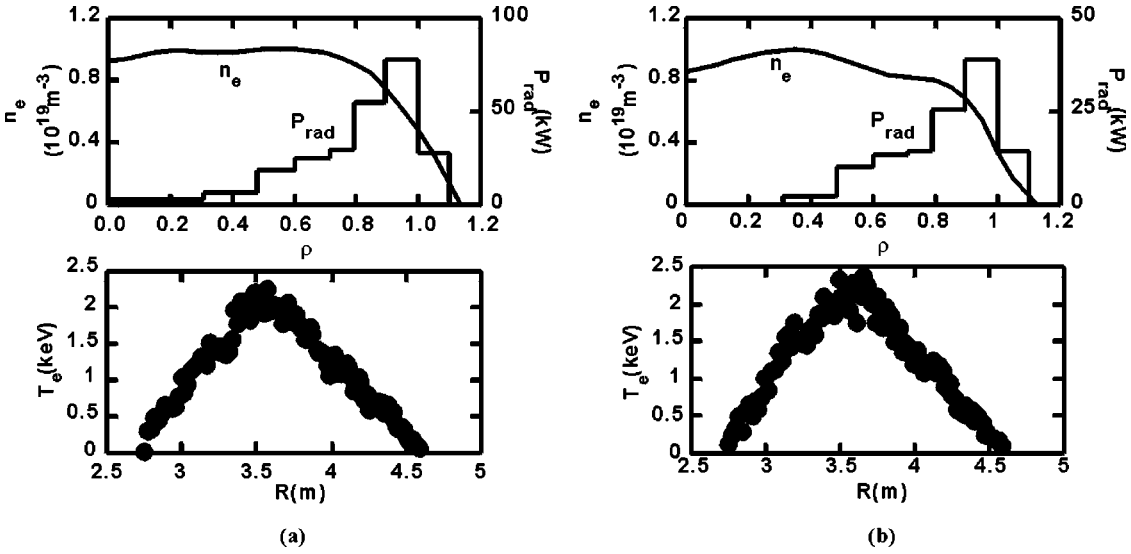

FIG. 7. A comparison of radial profiles of ICRF heated plasma with those of NBI heated plasma. (a) Radial profiles of the electron density, radiation and electron temperature for ICRF heated plasma. (b) Radial profiles of the electron density, radiation and electron temperature for NBI heated plasma.

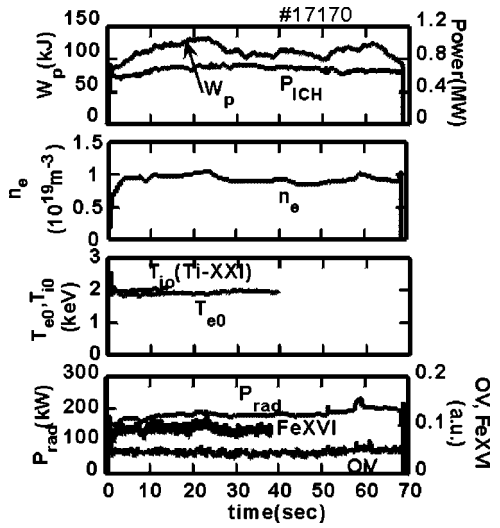

FIG. 8. Dependence of fusion triple product $n\tau_E T_{i0}$ on $n_e^{1.08} P_{\mathrm{ICH}}^{-0.18}$.

confinement, which was obtained at a relatively low electron density.

E. Long pulse of ICH-sustained plasma

A long-pulse operation was tried at the end of the third experimental campaign, using ICRF heating. The pulse length was lengthened shot by shot from 5 to 45 seconds in order to age the tetrode tubes of the final amplifier. The pulse duration time of ICH-sustained plasma was able to be prolonged up to 68 seconds as shown in Fig. 8. The radiated rf power from the antennas, the average plasma stored energy, the line average electron density, the electron temperature on the magnetic axis, the ion temperature and the radiation power are $P_{\mathrm{ICH}}=0.7\,\mathrm{MW}$, $W_p=110\,\mathrm{kJ}$, $n_e=1.0\times10^{19}\,\mathrm{m}^{-3}$, $T_{e0}=2.0\,\mathrm{keV}$, $T_{i0}=2.0\,\mathrm{keV}$ and $P_{\mathrm{rad}}=200\,\mathrm{kW}$, respectively. The ion temperature was measured from Doppler broadening of TiXXI (0.261 nm) using an x-ray crystal spectrometer.[24] The minority fraction was kept constant at $\mathrm{H}\alpha/\mathrm{HeI}=0.7$ and the impurity accumulation of FeXVI and OV was not observed during the long-pulse operation as shown in the bottom of Fig. 8. The energy confinement time and the operation time are given $\tau_E=0.19$ seconds and 68 seconds, respectively, and the fusion triple product is $n_e\tau_E T_{i0}=3.8\times10^{18}\,\mathrm{m}^{-3}\,\mathrm{keV\,s}$. The first goal of the steady-state discharge in the LHD is $n_e\tau_E T_{i0}=1.5\times10^{19}\,\mathrm{m}^{-3}\,\mathrm{keV\,s}$. It can be achieved at a higher electron density, e.g., $n_e=4\times10^{19}\,\mathrm{m}^{-3}$ at a $1\sim2$ MW level of the ICRF heating power, rather lower than 3 MW, which has been predicted to be required to achieve the objective of the LHD project; this will be discussed in the next section.

F. Parameters of ICRF heated plasma

A scaling of a fusion triple product is derived from ISS95 in the following equation:

$$n_e\tau_E T_{i0}(\times10^{20}\,\mathrm{m}^{-3}\,\mathrm{keV\,see}) = \mathrm{const}\times n_e(\times10^{19}\,\mathrm{m}^{-3})^{1.02} P_{\mathrm{ICH}}(\mathrm{MW})^{-0.18}. \quad (1)$$

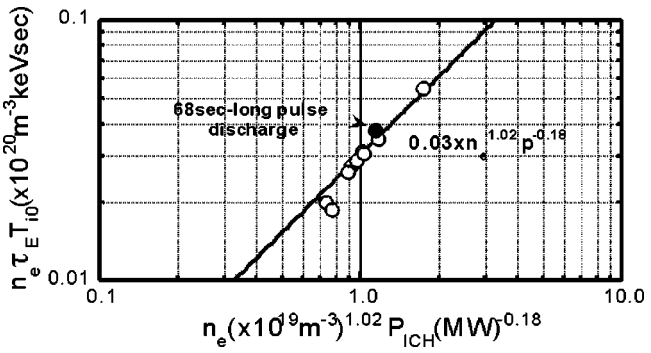

FIG. 9. Time evolutions of parameters of the long pulse plasma sustained by ICRF heating with $P_{\mathrm{ICH}}=0.7$ MW only.

To determine the numerical factor experimental data are plotted in Fig. 9 whose abscissa and ordinate are $n_e(\times10^{19}\,\mathrm{m}^{-3})^{1.02}\ P_{\mathrm{ICH}}(\mathrm{MW})^{-0.18}$ and $n_e\tau_E T_{i0}(\times10^{20}\,\mathrm{m}^{-3}\,\mathrm{keV\,s})$, respectively. The experimental range of the average electron density and the ICRF heating power are $0.75\times10^{19}\,\mathrm{m}^{-3}<n_e<1.8\times10^{19}\,\mathrm{m}^{-3}$ and $0.69\,\mathrm{MW}<P_{\mathrm{ICH}}<1.3\,\mathrm{MW}$, respectively. The numerical factor can be determined to be 0.03 from this figure. The fusion triple product of the long-pulse discharge (described in *E*) is also plotted using a solid circle.

The density limit is another interest in reactor relevant plasmas, because the fusion triple product is almost proportional to the electron density as described above. The electron density of the ICRF heated plasma discharge so far achieved is $n_e=1.8\times10^{19}\,\mathrm{m}^{-3}$. The density limit obtained in medium size of Heliotron and Stellarator devices[25] predicts $n_e=4\times10^{19}\,\mathrm{m}^{-3}$ at $P_{\mathrm{ICH}}=1.3\,\mathrm{MW}$. The achieved domain of the electron density is far below the density limit; therefore, a trial of the higher electron density discharge of ICRF heated plasma will be an important issue in the coming experimental campaign.

IV. HIGH ENERGY ION BEHAVIOR

A. Improved orbit of high energy ions

One of the major concerns in heliotron systems is whether high energy ions can be confined or not, due to the nonaxisymmetric magnetic configuration. As described in the previous section, one of the main reasons of the successful ICRF heating may be the improvement of the particle orbit of the trapped high energy ions accelerated by ICRF electric field. The position of the magnetic axis, R_{ax} is a key parameter determining the behavior of the deeply trapped ions and the MHD stability aspect. The inward-shifted configuration reduces the deviation of the particle orbit from the magnetic surface but deteriorates the MHD stability. The standard configuration has been selected to be $R_{\mathrm{ax}}=3.7$ m as a compromise. When the orbits of ions with perpendicular pitch angle are compared between the different magnetic axis configurations, i.e., $R_{\mathrm{ax}}=3.75$ m and $=3.6$ m, the improvement of the drift surface of a trapped particle is remarkable in the inward-shifted configuration.[26] In the coming 4th experimental campaign, it will be interesting to compare the

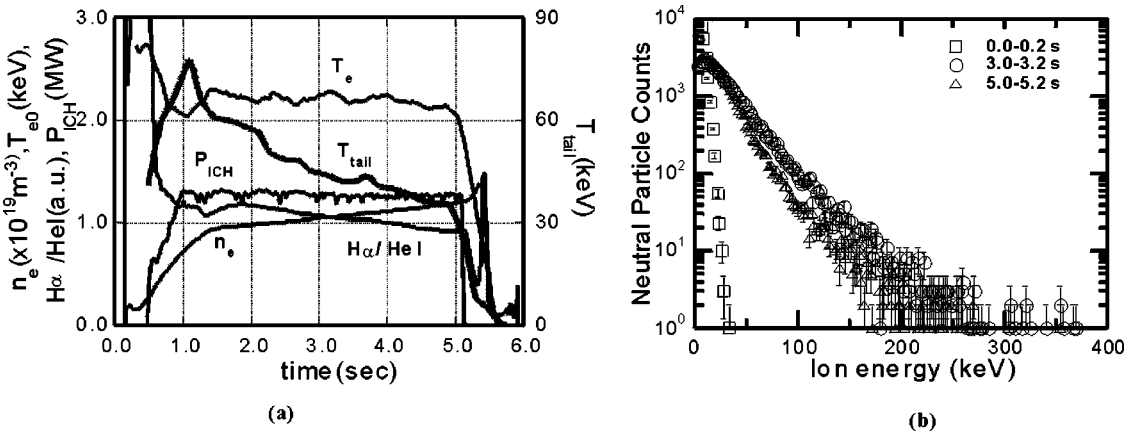

FIG. 10. High energy ion measurement using NDD: (a) Time evolutions of parameters of ICRF heated plasma with ICRF heating power and measure tail temperature T_{tail} in the energy range from 30 to 250 keV. (b) Counts number of high energy particle in the energy range from 30 keV to 250 keV during 0.2 seconds in three different periods.

ICRF heated plasma performance and the transfer efficiency (see Sec. IV C) among $R_{ax}=3.6$ m, $=3.75$ m and further outward shifted $R_{ax}=3.9$ m.

As described in Sec. III A, the heating efficiency is lower at $\omega/\omega_{ci}=1.01$ than at $\omega/\omega_{ci}=0.92$; however, the enhancement of the energy confinement time is the same, as shown in Fig. 2(b). The lower heating efficiency can be also explained by comparing the orbit of the high energy ions perpendicularly accelerated by the rf field. The trajectory of ions with the pitch angle of 90 degrees at $\omega/\omega_{ci}=0.92$ is poloidally and toroidally along the minimum magnetic field strength. These ions behave as deeply trapped particles in the helical ripple and are confined well in the case of the inward shifted configuration, i.e., $R_{ax}=3.6$ m. On the other hand, ions accelerated at $\omega/\omega_{ci}=1.01$ behave as transition particles referred to as ''trapped–detrapped particles.'' The trajectory is stochastic because such a particle is trapped in the helical ripple or in the toroidal ripple and sometimes becomes a passing particle without Coulomb collisions.[27] High energy ions with a pitch angle of 90 degrees at two ICRF heating conditions, i.e., $\omega/\omega_{ci}=0.92$ and $\omega/\omega_{ci}=1.01$ are categorized in 2 groups; transition particles and trapped particles. High energy ions with a pitch angle of 90 degrees at $\omega/\omega_{ci}=0.92$ are trapped particles and are well confined. On the other hand, perpendicularly accelerated ions at $\omega/\omega_{ci}=1.01$ are transition particles, which is the another reason for the lower heating efficiency, which was seen in Fig. 2(b).

B. Energy spectrum of high energy ions

The most successful ICRF heating has been achieved when the resonance layer of minority hydrogen ions was located at the saddle point on the mod-B surface (see Fig. 1). Most of the ICRF heated power was absorbed by the high energy ions.[18] A Natural Diamond Detector (NDD)[27,28] was installed to measure the high energy on tails and a fast particle neutral analyzer with a capability to separate the species by time of flight[29] was also equipped in the LHD. A spectrum of the high energy ions was measured by the NDD at the ICH-sustained plasma. Time evolutions of the plasma parameters and the ICRF heating power are shown in Fig. 10(a). The ICRF heating power ranges from 1.1 to 1.3 MW. The line average electron density and the electron temperature on the magnetic axis are $n_e=1.0\sim1.2\times10^{19}$ m^{-3} and $T_{e0}=2.2\sim2.1$ keV, respectively. The ratio of Hα/HeI gradually decreases from 1.2 to 0.9 with the increase in the electron density. The spectrum of high energy ions at 30–250 keV are shown in Fig. 10(b), where the gating time to count the neutral particle number is 0.2 seconds. In Fig. 10(b), three high energy ion spectra are shown in different periods of the discharge. Open squares show that of the ECH plasma in the first period, i.e., 0.0–0.2 s before ICRF power is turned on. Then open circles and open triangles are those of the ICRF heated plasma at 3.0–3.2 s and 5.0–5.2 s, respectively. The effective temperature of the high energy tail ions is derived from the ion energy spectrum, which is compared with that given by Stix's formula.[30,31] The effective ion temperature can be theoretically calculated from the following equation, which is derived from the energy balance between the ICRF absorbed power and the energy dissipation via the electron drag:

$$T_{\mathrm{eff}}=T_e\left(1+\frac{P_{\mathrm{abs}}\tau_s}{3n_HV_HT_e}\right). \tag{2}$$

Here P_{abs}, τ_s, n_H and V_H are the absorbed ICRF heating power, the Spitzer's slowing down time, the minority ion density and the heating volume respectively. Neglecting 1 in the bracket, T_{eff} is proportional to $P_{\mathrm{abs}}T_e^{1.5}/n_en_HV_H$. Figure 11 shows a comparison between the measured T_{tail} and the calculated T_{eff}. The minority ion density is difficult to measure but was deduced from the spectroscopic measurement of Hα and HeI. In the wide range of factor 2, T_{tail} agrees with the theoretical T_{eff}.[31] No saturation was observed up to $T_{\mathrm{tail}}=75$ keV in Fig. 11, indicating that the high energy ions were well confined so that the ion energy can be sufficiently transferred to electrons.

C. Enhancement of confinement time due to high energy ions and energy transfer efficiency

An enhancement of the energy confinement time due to the existence of high energy ions was expected on the basis

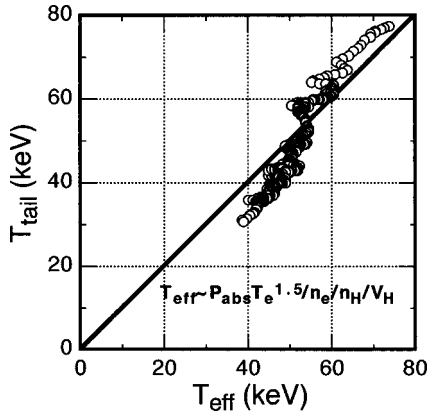

FIG. 11. A comparison of measured tail temperature T_{tail} with effective temperature calculated T_{eff} by Stix's formula.

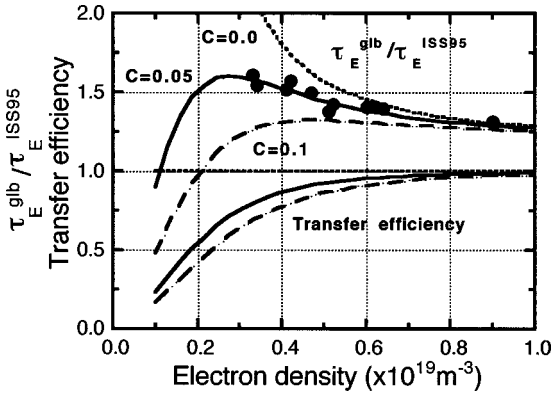

FIG. 12. Dependence of the enhancement of energy confinement time due to high energy ions on electron density at $P_{\mathrm{abs}}=0.5$ MW in three cases of $C=1.0$, 0.05 and 0.1. The transfer heating efficiency is also plotted.

of calculations of high energy ion orbits based on the Monte Carlo simulation.[26] The total plasma stored energy W_{tot} consists of two parts: one is the plasma stored energy of the bulk plasma W_{bulk} and the other is that of the high energy ion W_{tail}:

$$W_{\mathrm{tot}}=W_{\mathrm{bulk}}+W_{\mathrm{tail}}, \quad W_{\mathrm{tot}}=P_{\mathrm{total}}\tau_E^{\mathrm{glb}}, \quad W_{\mathrm{bulk}}=P_{\mathrm{trns}}\tau_E^{\mathrm{bulk}} \text{ and } W_{\mathrm{tail}}=P_{\mathrm{abs}}\tau_E^{\mathrm{tail}}. \tag{3}$$

The ICRF heating power is first absorbed by minority ions and then the high energy ion tail is formed. The bulk plasma is heated by the high energy ions via the electron slowing down process. Here P_{total}, P_{abs} and P_{trns} are the total heating power, the absorbed power by high energy ion and the transferred power to the bulk plasma, respectively. In the case of the experiment, P_{total} is the same as P_{abs}. τ_E^{total}, τ_E^{bulk} and τ_E^{tail} are the global energy confinement time, the energy confinement times of the bulk plasma and the high energy ions, respectively. τ_E^{tail} is given by $\tau_E^{\mathrm{tail}}=\eta\tau_s/2$, when the power transfer efficiency η is employed as $\eta=P_{\mathrm{trns}}/P_{\mathrm{abs}}$. The global energy confinement time is written in the following equation:

$$\tau_E^{\mathrm{glb}}=\eta\left(\tau_E^{\mathrm{bulk}}+\frac{\tau_s}{2}\right). \tag{4}$$

On the other hand, the scaling of the power transfer efficiency was formulated with the Monte Carlo simulation in the following form:

$$\eta=\frac{1}{1+CP_{\mathrm{abs}}{}^{\alpha}T_e^{\beta}n^{-\gamma}B^{-\delta}}. \tag{5}$$

The orbit loss crossing the last closed magnetic surface is regarded as the energy loss of the high energy ions. The exponents of α, β, γ and δ have been determined as $\alpha=1$, $\beta=2$, $\gamma=2$ and $\delta=1$. A numerical factor C depends on the ratio of minority ions, species of minority ions and a dimension of the device, etc. An enhancement of the global confinement time from that of ISS95 is expected in accordance with Eq. (4). When the transfer efficiency is $\eta=1.0$, the confinement enhancement may be found to be more than 10 at the longer τ_s, i.e., at the lower electron density. It is plotted against the electron density for the ICRF heating discharges, i.e., $P_{\mathrm{abs}}=0.5$ MW in Fig. 12. The increase in the normalized ratio of the global energy confinement time is observed in the lower electron density discharge. The enhancement, however, is smaller than that estimated in the case of $\eta=1.0$, which causes a lower transfer efficiency in the lower electron density discharge. The transfer efficiency can be deduced from the experimental data. In the analysis the average electron temperature is calculated from the bulk plasma confinement time, which obeys ISS95 with an enhancement factor. In Fig. 12, the estimated enhancement of the confinement time is plotted in three cases of the numerical factor C in Eq. (5), i.e., $C=0.0$ ($\eta=1.0$), $C=0.05$ and $C=0.1$. The transfer efficiency can be determined by fitting the experimental enhancement factor in the following form:

$$\eta=\frac{1}{1+0.05P_{\mathrm{abs}}T_e^2n^{-2}}. \tag{6}$$

The electron temperature measured at the half-radius of the plasma agrees well with the calculated electron temperature. It is also of interest to compare the transfer efficiency with that deduced by the Monte Carlo simulation, in which the bulk plasma is the same as in the experiment. The transfer efficiency agrees well with that of the simulation; however, the experimental one is a little lower than that of the simulation. The difference between them may be derived from the other loss process, which is not included in the Monte Carlo simulation, e.g., the charge exchange loss near the plasma edge.

One of the final goals of ICRF heating is an achievement of the high power heating at 10 MW. The scaling of the transfer efficiency with the Monte Carlo simulation can predict whether the ICRF heating at 10 MW will be successful or not in the future experiment. Figure 13 gives an answer to this question; the transfer efficiency is improved to 95% even at 10 MW of ICRF heating, when the electron density is increased to $4\times10^{19}\,\mathrm{m}^{-3}$.

V. SUMMARY

Results of ICRF heating experiments on the LHD were summarized with regard to two topics.

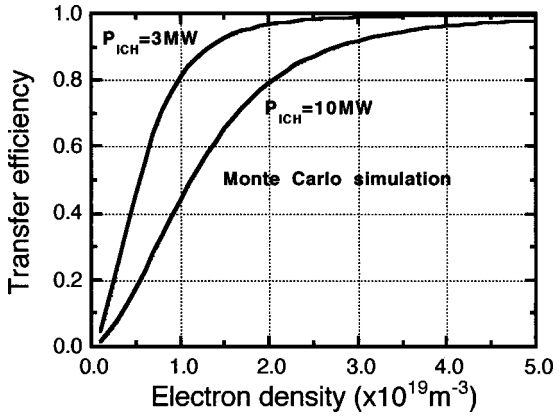

FIG. 13. Dependence of transfer efficiency on the electron densities in two cases of ICRF heating power of 3 MW and 10 MW. Experimental data are plotted using solid circles.

(1) The ICRF heating experiments demonstrated significant results with regard to the additional heating to the NNBI plasma, and the ICH-sustained plasma with high stored energy up to 200 kJ and at a long pulse of 68 seconds at 1 MW level. The ICRF heating power was mostly absorbed by minority protons in the optimized ICRF heating. The confinement characteristics of the ICRF heated plasma are the same as those of the NBI plasma. The energy confinement time is longer by a factor of 1.5 than that of ISS95.

(2) The deeply trapped high energy ions accelerated by the ICRF electric field were observed to be confined well by measuring the energy spectrum up to 250 keV. The tail ion temperature scales with Stix's formula, which may result from employing the configuration of the inward-shifted magnetic axis. The dependence of the transfer efficiency of the high energy tail ion to the bulk plasma on the electron density was experimentally obtained and it was found to agree fairly well with that of the Monte Carlo simulation. This result suggests that the ICRF heating will be successful even at 10 MW at an electron density of more than $4\times10^{19}\,\mathrm{m}^{-3}$.

Impurity accumulation was not observed in the whole ICRF heated plasma, and this is thought to result from the installation of carbon divertor plates and a forementioned improvement in the high energy particle confinement due to the inward shifted R_{ax}.

Three more identical antennas will be installed to double or triple the ICRF heating power in the coming experimental campaign. A long-pulse operation more than 5 minutes will be tried at the higher fusion triple product, e.g., $n_e\tau_E T_{i0}=1.0\sim1.5\times10^{19}\,\mathrm{m}^{-3}\,\mathrm{keV\,sec}$ in the coming experimental campaign of 2000.

ACKNOWLEDGMENTS

The authors would like to thank the scientists and the technical staff at the National Institute for Fusion Science who made these experiments possible and especially the former director-general, Professor A. Iiyoshi.

[1]R. Kumazawa, T. Mutoh, T. Seki *et al.*, J. Plasma Fusion Res. **3**, 352 (2000).
[2]O. Motojima, K. Akaishi, K. Fujii *et al.*, Fusion Eng. Des. **20**, 3 (1993).
[3]O. Motojima, K. Akaishi, H. Chikaraishi *et al.*, Nucl. Fusion **40**, 599 (2000).
[4]M. Fujiwara A. Iiyoshi, A. Komori *et al.*, Nucl. Fusion **39**, 1245 (1999).
[5]M. Fujiwara, K. Kawahata, N. Ohyabu *et al.*, to be published in *Proceedings of the 18th IAEA Fusion Energy Conference*, OV 1/4 (International Atomic Energy Agency, Vienna, 2000).
[6]A. Komori, Bull. Am. Phys. Soc. **45**, 289 (2000).
[7]R. Kumazawa, T. Mutoh, T. Watari, T. Seki, F. Shimpo, and G. Nomura, *Proceedings of the 18th Symposium on Fusion Technology* (International Atomic Energy Agency, Vienna, 1996), Vol. 1, p. 617.
[8]T. Watari, T. Shimozuma, Y. Takei *et al.*, *Proceedings of 17th Fusion Energy*, 1998, Vol. 4, p. 1293.
[9]R. Kumazawa T. Mutoh, T. Seki, F. Shimpo, G. Nomura, T. Ido, T. Watari, J-M. Noterdaeme, and Y. Zhao, Rev. Sci. Instrum. **70**, 555 (1999).
[10]T. Mutoh, R. Kumazawa, T. Seki, F. Shimpo, G. Nomura, T. Ido, T. Watari, J-M. Noterdaeme, and Y. Zhao, Fusion Eng. Des. **26**, 387 (1999).
[11]R. Kumazawa T. Mutoh, T. Seki, F. Shimpo, G. Nomura, T. Ido, T. Watari, J-M. Noterdaeme, and Y. Zhao, J. Plasma Fusion Res. **75**, 842 (1999).
[12]T. Seki, R. Kumazawa T. Mutoh, F. Shimpo, G. Nomura, T. Yasui, K. Saito, Y. Torii, and T. Watari, J. Plasma Fusion Res. **3**, 359 (2000).
[13]R. Kumazawa, T. Mutoh, T. Seki *et al.*, *13th Topical Conference on Radio Frequency Power in Plasmas*, 1999, Vol. 485, p. 160.
[14]T. Mutoh, R. Kumazawa, T. Seki *et al.*, Plasma Phys. Controlled Fusion **42**, 265 (2000).
[15]T. Seki, R. Kumazawa, T. Mutoh *et al.*, to be published in *Proceedings of the 27th European Conference on Controlled Fusion and Plasma Physics* (European Physical Society, Petit-Lancy, 2000).
[16]R. Kumazawa, K. Nishimura, T. Mutoh *et al.*, *Proceedings of the 21st European Conference on Controlled Fusion and Plasma Physics*, 1994, Part II, p. 1000.
[17]S. Masuda, R. Kumazawa, K. Nishimura *et al.*, Nucl. Fusion **37**, 53 (1997).
[18]K. Saito, R. Kumazawa, T. Mutoh *et al.*, to be published in Nucl. Fusion.
[19]U. Stroth, M. Murakami, R. A. Dorry, H. Yamada, S. Okamura, F. Sano, and T. Obiki, Nucl. Fusion **36**, 1063 (1996).
[20]M. Osakabe, Y. Takeiri, K. Tsumori *et al.*, be published in Rev. Sci. Instrum.
[21]B. J. Peterson, Y. Nakamura, K. Yamazaki *et al.*, to be published in J. Nucl. Material.
[22]K. Narihara, I. Yamada, N. Ohyabu *et al.*, to be published in *Proceedings of the 18th IAEA Fusion Energy Conference*, EXP5/28, 2000.
[23]K. Kawahata, K. Tanaka, Y. Ito, A. Ejiri, and S. Okajima, Rev. Sci. Instrum. **70**, 707 (1999).
[24]S. Morita, Y. Ogawa, T. Watari, R. Akiyama, K. Kadota, Y. Kawasumi, T. Ozaki, M. Sasao, and K. Sato, *Proceedings of the 14th European Conference on Controlled Fusion and Plasma Physics* (European Physical Society, Petit-Lancy, 1987), Part III, p. 874.
[25]S. Sudo, Y. Takeiri, H. Zushi, F. Sano, K. Itoh, K. Kondo, and A. Iiyoshi, Nucl. Fusion **30**, 11 (1990).
[26]S. Murakami, N. Nakajima, M. Okamoto, and J. Nuhrenberg, Nucl. Fusion **39**, 1165 (1999).
[27]M. Sasao, S. Murakami, M. Isobe *et al.*, to be published in the Ref. 27, EX9/1, 2000.
[28]A. V. Krasilnikov, S. S. Medley, N. N. Gorenkov, R. V. Bundy, D. S. Darrow, and A. L. Roquemore, Nucl. Fusion **39**, 1111 (1999).
[29]T. Ozaki, V. Zanza, G. Bracco *et al.*, Rev. Sci. Instrum. **71**, 2698 (2000).
[30]T. H. Stix, Nucl. Fusion **15**, 737 (1975).
[31]T. Mutoh, R. Kumazawa, T. Seki *et al.*, Phys. Rev. Lett. **85**, 4530 (2000).